Check for updates

Mitigating voltage losses in photoelectrochemical cell scale-up†

Fatwa F. Abdi, [ID] *[a] Ronald Ramiro Gutierrez Perez[b] and Sophia Haussener [ID] [b]

In solar water splitting, efforts in scaling up the photoelectrochemical cell beyond laboratory scale have started to attract significant attention. Several large-area devices have been demonstrated, but typically the efficiencies are much lower than their small-area equivalent. Here, two-dimensional finite element modeling is used to evaluate the different sources of voltage loss specifically related to scale-up in solar water splitting devices operated in neutral pH solutions. We quantitatively investigate the influence of the electrode area to these scale-up associated losses (substrate ohmic loss, electrolyte ohmic loss, and local pH-gradient related losses). About 600 mV additional overpotential is needed due to these losses for a cell with electrodes of height of 8 cm at a current density of 10 mA cm^{-2}. We show, however, that by applying engineering and cell design strategies, the voltage losses can be mitigated, resulting in an acceptable ∼50 mV overpotential. Overall, this study highlights the additional challenges to be considered in photoelectrochemical cell scale-up and provides strategies to manage and mitigate scaling-related losses.

Introduction

The progress in photoelectrode materials development for solar water splitting in the past 10–15 years has resulted in numerous demonstrations of unassisted solar water splitting devices. Various architectures have been utilized and solar-to-hydrogen (STH) efficiencies as high as 30% have been reported.[1–4] Unfortunately, the high efficiencies (>15%) have only been demonstrated using expensive and scarce III–V semiconductors,[5–8] which are challenging to be scaled up to the GW or TW level, unless concentrated irradiation is considered.[9] On the other hand, relatively low-cost oxide-based devices have only achieved STH efficiency of ∼8%.[10–12] These oxide-based devices typically use BiVO$_4$ as the top-absorber in a tandem configuration, and the theoretical maximum for such a device is only ∼9%, limited by the 2.4 eV bandgap absorption of BiVO$_4$. Significant research efforts are therefore directed towards developing novel complex oxides with smaller bandgaps (1.7–1.9 eV) to replace BiVO$_4$.[13–18]

In addition, given the impressive development of solar water splitting devices, the next step is to shift beyond the laboratory experiments and demonstrate large-scale devices. Scaling can be quantified by the power of a device and can be increased by concentrating the solar irradiation or by increasing the photoabsorber area. The latter is more commonly done. Large-area demonstrations have started to emerge in the past few years, but the number is still very limited. Most reported devices have an area of smaller than 1 cm^2, and only a handful demonstrated areas larger than 10 cm^2.[2,19–23] Moreover, these large-area devices tend to deliver much lower STH efficiency (by up to a factor of ∼5) as compared to their small-area equivalent.[2] For example, it was recently reported that while small-area (0.24 cm^2) BiVO$_4$-based tandem device delivers STH efficiency of ∼6%, the large-area (50 cm^2) equivalent is only capable of delivering an STH efficiency of ∼2%.[21] The significant loss of efficiency has been attributed not to the scale-up of the light absorber material (*i.e.*, BiVO$_4$) itself, but more to the ohmic losses and mass-transport (proton/hydroxyl ions) limitations. Several modeling studies have also investigated some of these aspects (substrate losses, ionic drop, mass transfer),[24–28] but the overall quantification of the various loss mechanisms related to scale-up has not been reported. This is important in order to propose and implement appropriate (photo)electrochemical engineering and design strategies in order to overcome the scale-up related losses.

Here, we use two-dimensional (2-D) finite element modeling to quantify the different scale-up related loss mechanisms in a solar-water splitting device: substrate ohmic loss, electrolyte ohmic loss, and local pH-gradient related losses. We consider a membrane-less water splitting device, where the product (*i.e.*, O$_2$ and H$_2$) separation is done using hydrodynamic control,[29,30] operated with buffered electrolyte

[a]Institute for Solar Fuels, Helmholtz-Zentrum Berlin für Materialien und Energie GmbH, Hahn-Meitner-Platz 1, Berlin 14109, Germany. E-mail: fatwa.abdi@helmholtz-berlin.de

[b]Laboratory of Renewable Energy Science and Engineering, Institute of Mechanical Engineering, École Polytechnique Fédérale de Lausanne, 1015 Lausanne, Switzerland

† Electronic supplementary information (ESI) available: ESI Note on governing equations, Table S1 on baseline parameters and Fig. S1–S10. See DOI: 10.1039/d0se00246a

at neutral pH. Although the use of neutral pH increases the potential drop in the cell (*i.e.*, due to the evolving pH-gradient and the associated overpotentials), a device operating at neutral pH allows the use of abundant seawater and is safer to operate over large collection areas. Also, many earth-abundant light absorbers and catalysts are unstable in acidic or alkaline electrolytes.[31–33] The influence of electrode area to the scale-up associated losses is investigated. Finally, we offer engineering and design strategies in order to manage and mitigate the overall voltage losses.

Model description and boundary conditions

Fig. 1 illustrates the 2-D schematic of the cell geometry used in this study, *i.e.*, a membrane-less planar two-electrode configuration. In such a configuration, hydrodynamic flow alone is sufficient to separate the products and ensure safe operation without the use of conventional membranes.[29,30] Since it has been shown that the voltage losses associated with scale-up are not due to additional potential drop within the light absorbers,[21] only dark electrochemical reactions are taken into consideration here. For our analysis to be valid, the resistance of the semiconductor layer itself should therefore be negligible and the deposition at large area should still result in homogenous films. The baseline parameters used in our simulations are tabulated in Table S1 (ESI†). COMSOL Multiphysics® was used to solve the governing conservation and transport equations (see ESI Note 1† for details).
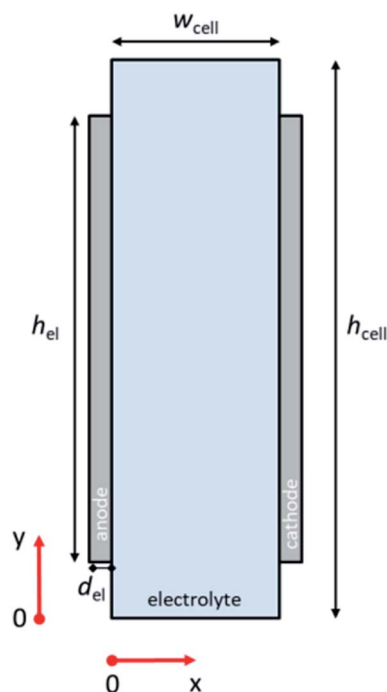

Fig. 1 Schematic of the computational domain consisting of the liquid electrolyte and the two solid electrodes: h_{cell} = cell height, w_{cell} = cell width, h_{el} = electrode height, d_{el} = electrode thickness.

The computational domain consisted of the liquid electrolyte channel of different widths (w_{cell}) and heights (h_{cell}) between the two solid electrodes of a given thickness (d_{el}) and of different heights (h_{el}). Assuming the density (ρ) and dynamic viscosity (μ) of the electrolyte to be equal to those of water, and considering all the combinations of cell widths (w_{cell}) and inlet velocities ($v_y = v_{in}$) used in this study, the maximum Reynolds number (Re) is 1200, so that laminar flow can be assumed. Re values for the various w_{cell} and v_{in} investigated in this study are shown in Fig. S1;† all remain below the laminar-to-turbulence transition value (*i.e.*, 2000). The solution of the mass conservation and Navier–Stokes equation provided a parabolic velocity profile. The boundary conditions consisted of an inlet velocity v_{in} normal to the inlet with developed flow (*i.e.* an entrance length of 1 cm was used). The pressure of the top boundary of the electrolyte is fixed (p_{out}). At the walls of the cell, no-slip boundary conditions ($v_x = v_y = 0$) were used.

The transport of ionic species was calculated in a diluted solution by solving the Nernst–Planck equation for the following species: H^+, K^+, HPO_4^{2-}, and $H_2PO_4^-$. The concentration of dissolved gases was calculated by solving the diffusion–advection equation for O_2 and H_2 in water. Diffusion coefficients of the various species are indicated in Table S1.† Concentration-dependent Butler–Volmer equations were solved at the electrode–electrolyte interface, using potential–current characteristics on the surface of the anode and cathode. Kinetic values representative of state-of-the-art catalysts (Pt for HER and RuO_2 for OER)[27,34–37] were used (see Table S1†). Constant concentration for the ionic species ($c_i = c_{0,i}$) and zero concentration for H_2 and O_2 were set at the inlet, and no diffusive outflow ($nD_i\nabla c_i = 0$) at the outlet. 2 M potassium phosphate (KP_i) buffer was considered for this study, and the following equilibrium reaction with the respective equilibrium constant is considered:

$$HPO_4^{2-} + H^+ \rightleftharpoons H_2PO_4^-, \quad K_{eq} = 1.5 \times 10^{-4} \text{ mol m}^{-3} \quad (1)$$

Charge conservation and transport was solved in the electrolyte. Average current density was applied at the anode's electrical contact. The potential of the cathode's electrical contact was set to ground (see Fig. S2†). The edges at which no flux ($-nJ_i = 0$) and insulation ($-ni_s = 0$) boundary conditions were used are also specified in Fig. S2.† The electrode's conductivity (σ_{el}) of 10^5 S m^{-1} was used as a typical value for a transparent conducting oxide (TCO) substrate. Although the typical thickness of TCO is in the order of 500 nm, we used a 1 mm pseudo-domain to represent the film thickness to avoid meshing complexity at the interface. Anisotropic conductivity (σ_s), eqn (2)–(4), and scaling factors were applied in order to ensure that the difference between the real thickness ($d_{el,0}$) and the pseudo-domain thickness (d_{el}) does not affect the simulation.

$$\sigma_s = \begin{bmatrix} \sigma_x & 0 \\ 0 & \sigma_y \end{bmatrix} \quad (2)$$

$$\sigma_x = \frac{\sigma_{el} d_{el}}{d_{el,0}} \tag{3}$$

$$\sigma_y = \frac{\sigma_{el} d_{el,0}}{d_{el}} \tag{4}$$

The total cell voltage (V_{cell}) is the sum of the equilibrium potential (E_{eq}), the kinetic overpotentials for the oxygen and hydrogen evolution reactions (η_{OER} and η_{HER}), the ohmic loss in the substrate ($V_{ohmic,substrate}$), the ohmic loss in the electrolyte ($V_{ohmic,electrolyte}$), and the Nernstian loss due to pH gradients at the surface of the electrodes ($V_{pH\ grad}$).

$$V_{cell} = E_{eq} + \eta_{OER} - \eta_{HER} + V_{ohmic,substrate}$$
$$+ V_{ohmic,electrolyte} + V_{pH\ grad} \tag{5}$$

E_{eq}, η_{OER}, and η_{HER} are not affected by scaling up of the electrodes; the values are therefore not reported here. The following equations describe the three voltage losses considered in this study.

$$V_{ohmic,substrate} = V_{ohmic,substrate-anode} + V_{ohmic,substrate-cathode} \tag{6}$$

$$V_{ohmic,electrolyte} = V_{electrolyte,anode} - V_{electrolyte,cathode} \tag{7}$$

$$V_{pH\ grad} = V_{pH\ grad-anode} + V_{pH\ grad-cathode}$$
$$= 2.303\ \frac{RT}{F}(pH_{cathode} - pH_{anode}) \tag{8}$$

R is the gas constant, T is the absolute temperature and F is the Faraday constant (96 485 C mol^{-1}). The schematic illustration of these losses in the cell is shown in Fig. S3.†

100% faradaic conversion efficiency to H$_2$ and O$_2$ was assumed at the surface of the cathode and anode, respectively. The local current at the electrode surface (i_{loc}) was coupled with the generation rate (R_i, see also eqn (S1)†) of H$_2$ and O$_2$.

$$R_i = \frac{-\nu_i i_{loc}}{nF} \tag{9}$$

ν_i is the stoichiometry coefficient of the redox equilibrium reaction for species i, n is the number of participating electrons (2 for H$_2$ generation and 4 for O$_2$). Bubble formation is not considered in this study; therefore, the laminar flow is not disrupted. On the other hand, super-saturation of the electrolyte with dissolved H$_2$ and O$_2$ is assumed; indeed, supersaturation of dissolved H$_2$ by a factor of 50 has been experimentally measured.[38]

All the geometry was meshed with free triangular elements. The maximum mesh element size and the relative tolerance for the simulation were studied in order to minimize the relative error of electrode potential and local current density. The results are shown in Fig. S4† in which the chosen mesh (quantified through the maximal mesh element size) and relative tolerance for our simulations are identified. The optimized mesh configuration used in our study is shown in Fig. S5.† Steady-state solutions were obtained using the multifrontal massively parallel sparse (MUMPS) direct solver of COMSOL Multiphysics®. A minimum inlet velocity, ν_{in}, of 0.27 cm s^{-1} was needed in order to obtain convergence of the steady-state solution, as the input flux of the electrolyte is not sufficient to reach an equilibrium. When ν_{in} is lower than this value, voltage losses can only be evaluated for a period of time, but steady-state solution cannot be obtained (see Fig. S6†).

Results and discussions

Fig. 2 shows the voltage losses associated with scaling up the electrode height from 0.3 to 8 cm in 2 M KP$_i$ buffer electrolyte (pH 7). The average current density at the surface of the electrodes ($j_{app,s}$) was set to 10 mA cm^{-2}, and the inlet electrolyte velocity (ν_{in}) was 0.27 cm s^{-1}. Three different sources of voltage loss are identified: $V_{ohmic,substrate}$, $V_{pH\ grad}$, and $V_{ohmic,electrolyte}$ (see eqn (6)–(8)). $V_{ohmic,electrolyte}$ is found to be the least affected by the electrode size; it remains less than 100 mV even for the largest electrode height of 8 cm. The pH gradient and the associated $V_{pH\ grad}$ increase with increasing electrode height, which results from the inability to replenish protons at the region close to the surface of the electrodes. The largest voltage loss is $V_{ohmic,substrate}$, due to the limited conductivity of the substrate ($\sigma_{el} = 10^5$ S m^{-1}). For the 8 cm electrode, the $V_{ohmic,substrate}$ value is as high as 350 mV. Overall, the total voltage loss is shown to be significantly increased with increasing electrode height, from ~50 mV for the 0.3 cm electrode to ~600 mV for the 8 cm electrode. Such a substantial voltage loss is unacceptable for the operation of the overall water splitting device; this value needs to be minimized, ideally to a more acceptable level of 50–100 mV.
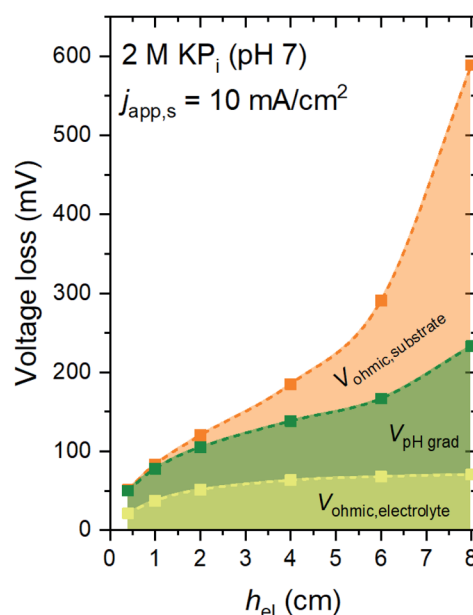

Fig. 2 Contribution of the electrolyte ohmic loss ($V_{ohmic,electrolyte}$), the pH gradient loss ($V_{pH\ grad}$), and the substrate ohmic loss ($V_{ohmic,substrate}$) as a function of the height of the electrode (h_{el}). The electrolyte is 2 M KP$_i$ buffer (pH 7). $j_{app,s} = 10$ mA cm^{-2}, $\nu_{in} = 0.27$ cm s^{-1}, $\sigma_{el} = 10^5$ S m^{-1}, $h_{cell} = 10$ cm, and $w_{cell} = 3$ cm.

Voltage losses in the substrates

We first consider minimizing and mitigating the $V_{\text{ohmic,substrate}}$. An obvious way is to replace the substrate with a more conductive material. Fig. 3a shows the influence of substrate conductivity on $V_{\text{ohmic,substrate}}$. At $j_{\text{app,s}} = 10$ mA cm^{-2}, replacing the substrate from FTO ($\sigma_{\text{el}} \sim 10^5$ S m^{-1}) to ITO ($\sigma_{\text{el}} \sim 10^6$ S m^{-1} (ref. 39–41)) significantly decreases $V_{\text{ohmic,substrate}}$ by a factor of $\sim$7. $V_{\text{ohmic,substrate}}$ can be further decreased to $\sim$10 mV when Ag is used as the substrate ($\sigma_{\text{el}} \sim 10^7$ S m^{-1} (ref. 42 and 43)). However, these high conductivity substrates may pose additional challenges. For example, in addition to being more expensive, ITO is less resistant to high temperature as compared to FTO; deposition of many thin-film semiconductors, especially metal oxides, typically require temperatures higher than 500 °C. Ag, on the other hand, is opaque. For an overall solar water splitting device that employs stacked tandem configurations, a transparent substrate is needed in order to allow the transmitted light from the first photoabsorber to reach the last photoabsorber. Spectrum splitting or a back reflector can be utilized for non-transparent tandem devices,[12,44,45] but the configuration is complicated and might be impractical. Alternatively, highly conductive metallic lines can be deposited on FTO substrates to improve the effective conductivity (see inset of Fig. 3b). Although these metallic lines would partially block the light, a much more significant reduction in ohmic losses (i.e., minimize $V_{\text{ohmic,substrate}}$) could be obtained. Fig. 3b shows the influence of the spacing between the metallic lines (d_{contact}) on $V_{\text{ohmic,substrate}}$. When d_{contact} is 2 cm or less, $V_{\text{ohmic,substrate}}$ can be decreased to <75 mV; this is a 5-fold reduction of voltage loss while only blocking $\sim$4% of the transmitted light (contact width, w_{contact}, of 1 mm). Indeed, this method has been employed in photovoltaic cells, where metallic busbars are deposited on the front contact of the cells.[46,47] Photocurrent improvements on 50 cm^2 BiVO$_4$ photoelectrodes

have also been demonstrated by depositing conducting nickel lines on top of the FTO substrates.[21]

Decreasing d_{contact} to less than 1 cm will further reduce $V_{\text{ohmic,substrate}}$. However, at the same time, a larger portion of the transmitted light will be blocked (see Fig. S7†). This can be overcome by decreasing w_{contact} to e.g., 0.5 mm, but it should be noted that the resistance of the metallic lines increases with decreasing w_{contact}, and voltage losses along the metallic lines can no longer be neglected. Overall, these two parameters (i.e., d_{contact} and w_{contact}) need to be specifically optimized depending on the type of metal and the current density, in light of the competing factors of blocked transmission and resistive losses in the metallic lines.

pH gradient losses

Fig. 4a shows the pH profile across the electrolyte, from the anode to the cathode (along the x-direction). Two pH profiles, at the bottom and the top of the electrode, are shown. At the anode side, water oxidation takes place and the accumulation of proton results in a local decrease of pH, while depletion of proton close to the cathode side, where water reduction occurs, causes a local pH increase. The pH variation is found to be limited to the vicinity of the surface (<2 mm away), and it is larger at the top of the electrode as compared to the bottom of the electrodes. This is a result of a constant supply of fresh electrolyte from the inlet, closer to the bottom of the electrodes. A color map of the pH of the electrolyte is shown in Fig. 4b. A maximum pH difference of $\sim$4.3 is observed, which corresponds to a voltage loss of $\sim$250 mV. This pH gradient can be minimized by increasing the inlet velocity (Fig. 4c). That is, increasing the mixing helps in reducing the pH gradient. Turbulence could further enhance this mixing effect and reduce the pH gradient, but at the same time increases the risks of products (O$_2$ and H$_2$) mixing. With increasing inlet velocity, the replenishment and transport of protons close to the anode and cathode surface, respectively, are promoted. This is in agreement with the "restricted" electrolyte volume effect recently demonstrated in an experimental study by Ahmet et al.[21] At an inlet velocity of 4 cm s^{-1}, the maximum pH difference is limited to $\sim$0.6 (Fig. 4d), which corresponds to a voltage loss of only $\sim$40 mV.

The dependence of $V_{\text{pH grad}}$ on the inlet velocity is summarized in Fig. 5 for an electrode of 8 cm height with a substrate that has conducting metal lines spaced at 1 cm distance (i.e., $d_{\text{contact}} = 1$ cm). Note that, for simplicity, $j_{\text{app,s}}$ is kept at 10 mA cm^{-2}. Increasing the inlet velocity dramatically decreases the pH gradient close to the electrodes' surface and the corresponding $V_{\text{pH grad}}$. $V_{\text{pH grad}}$ can be minimized to $\sim$20 mV by having an inlet velocity of 4 cm s^{-1}. The difference between this value to the one shown in Fig. 4c and d ($\sim$40 mV) suggests that there is a synergy between the application of conducting metal lines and increasing the inlet velocity. With the application of conducting metal lines, the local current density distribution at the surface of the electrodes becomes more uniform (Fig. S8a†). Similarly, with higher inlet velocity, a more uniform local current distribution is obtained (Fig. S8b†). As a result,
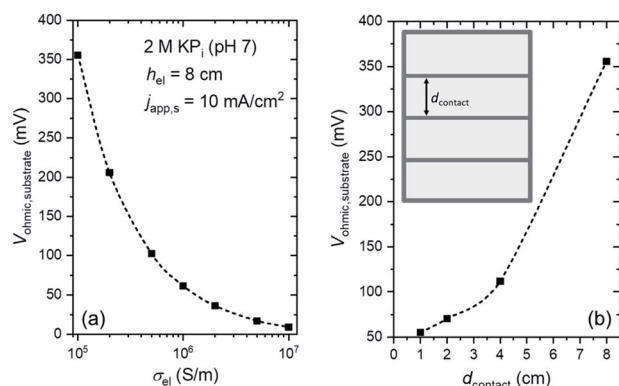

Fig. 3 Substrate ohmic voltage loss ($V_{\text{ohmic,substrate}}$) as a function of (a) the conductivity of the electrode and (b) the distance between metallic contacts (d_{contact}). The inset of (b) illustrates the metallic contacts on the substrate. In (a) $j_{\text{app,s}} = 10$ mA cm^{-2}, while it is adjusted in (b) to account for the radiation blocked by the opaque metallic lines (i.e., $j_{\text{app,s}}$ is reduced by 1.25%, 3.75% and 8.75% for d_{contact} of 4, 2 and 1 cm, respectively). The electrolyte is 2 M KP$_i$ buffer (pH 7). $v_{\text{in}} = 0.27$ cm s^{-1}, $h_{\text{el}} = 8$ cm, $h_{\text{cell}} = 10$ cm, and $w_{\text{cell}} = 3$ cm.
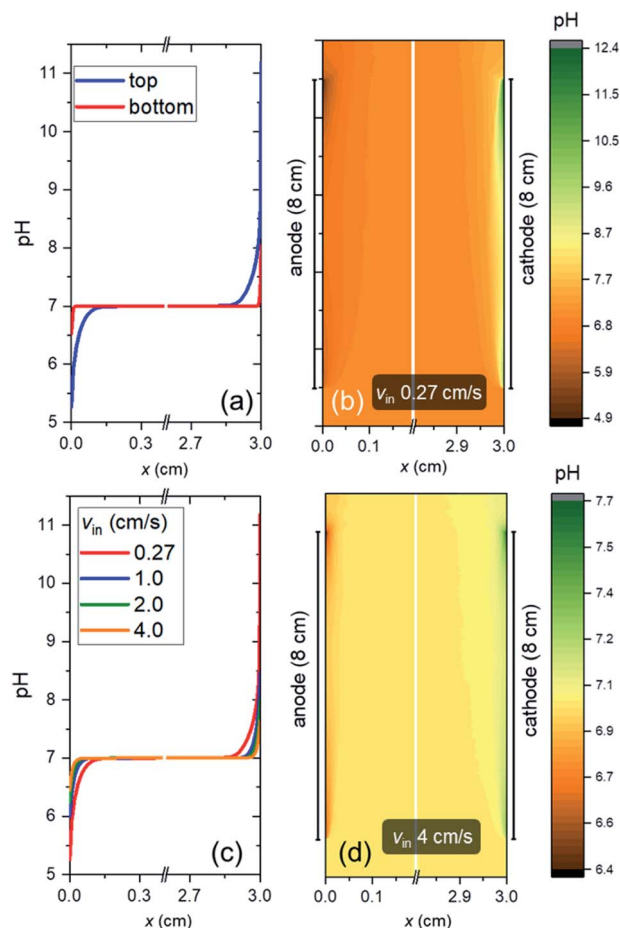
Fig. 4 (a) pH profile across the electrolyte (x-direction, from anode to cathode) at the top and bottom of the electrode at inlet velocity of 0.27 cm s^{-1}. (b) Colormap of pH in the electrolyte at inlet velocity of 0.27 cm s^{-1}. (c) pH profile across the electrolyte at the top of the electrode for various inlet velocities. (d) Colormap of pH in the electrolyte at inlet velocity of 4 cm s^{-1}. The electrolyte is 2 M KP$_i$ buffer (pH 7) and the substrate does not have any conducting metal lines. $j_{app,s}$ = 10 mA cm^{-2}, h_{el} = 8 cm, h_{cell} = 10 cm, and w_{cell} = 3 cm.

$V_{ohmic,substrate}$ is further minimized to ~15 mV for $d_{contact}$ = 1 cm and v_{in} = 4 cm s^{-1} (Fig. S8c†).

Electrolyte ohmic losses

With $V_{pH\ grad}$ and $V_{ohmic,substrate}$ minimized to a sum of ~35 mV, the electrolyte ohmic loss ($V_{ohmic,electrolyte}$) becomes the dominant contributor to the total voltage loss. $V_{ohmic,electrolyte}$ can be reduced by increasing the ionic conductivity of the electrolyte, i.e., by increasing the molarity of the phosphate buffer. However, the molarity used in this simulation (i.e., 2 M) is already very close to the solubility limit; it has been reported that concentrations of KP$_i$ higher than 2 M results in rapid precipitation of phosphate crystals on the walls of the cell.[21] Alternatively, one can reduce the distance between the anode and the cathode (i.e., w_{cell}). However, since a membrane-less configuration is used here, it has to be ensured that decreasing w_{cell} still results in no (or minimal) product cross-over. We calculated the percentages O$_2$ and H$_2$ cross-over (i.e.,
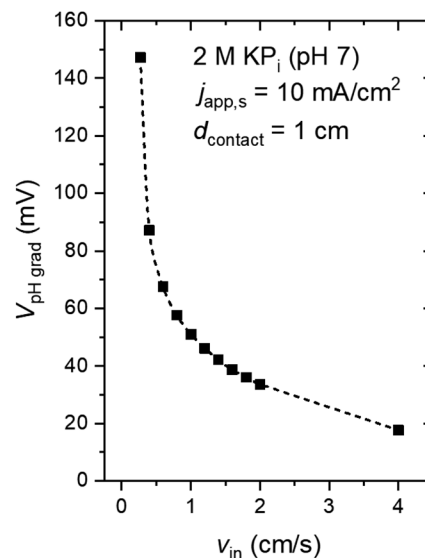

Fig. 5 Voltage loss associated with pH gradient ($V_{pH\ grad}$) as a function of the inlet velocity (v_{in}). The electrolyte is 2 M KP$_i$ buffer (pH 7). $j_{app,s}$ = 10 mA cm^{-2}, $d_{contact}$ = 1 cm, h_{el} = 8 cm, h_{cell} = 10 cm, and w_{cell} = 3 cm.

O$_2$ collected at the cathode outlet and H$_2$ collected at the anode outlet) with various w_{cell} and for various v_{in}, as shown in Fig. S9.† The amount of product cross-over increases with decreasing w_{cell}, but it is still less than 1% even for w_{cell} of 1 cm. A 1%-product concentration contour is also shown in Fig. S9b,† for the case of w_{cell} = 1 cm, indicating that more than 99% of H$_2$ and O$_2$ can be collected at the designated outlets.

We then combined the simple engineering and design parameter strategies (i.e., application of metallic lines, increasing inlet velocity and decreasing cell width) and examined the total voltage loss (Fig. 6a). At a current density of 10 mA cm^{-2}, the total voltage loss can be minimized to ~50 mV for w_{cell} = 1 cm, v_{in} = 4 cm s^{-1} and $d_{contact}$ = 1 cm. This amount of voltage loss is much more acceptable than the initial ~600 mV voltage loss (vide supra). Fig. 6b shows the contribution of each type of voltage loss for various current densities. Note that $V_{pH\ grad}$ is even further decreased (vs. the values in Fig. 5) because the smaller w_{cell} increases the electrolyte velocity closer to the surface of the electrodes. This increases the replenishment/transport rate of protons close to the surface of the electrodes and reduces the pH gradient further. As a result, both pH gradient and substrate conductivity are no longer the main limitations; instead, the electrolyte ohmic loss ($V_{ohmic,electrolyte}$) constitutes half of the total voltage loss. Other strategies to decrease the ionic resistance, e.g., introducing a conductive supporting electrolyte or using a highly conductive MEA configuration, need to be explored in order to minimize the voltage loss further.

Finally, we re-emphasize that our study does not take turbulence or multi-phase flow into consideration. While laminar flow is a valid assumption based on the Reynolds numbers for all examined conditions (vide supra), multi-phase flow induced mixing may enhance the mass transport, which
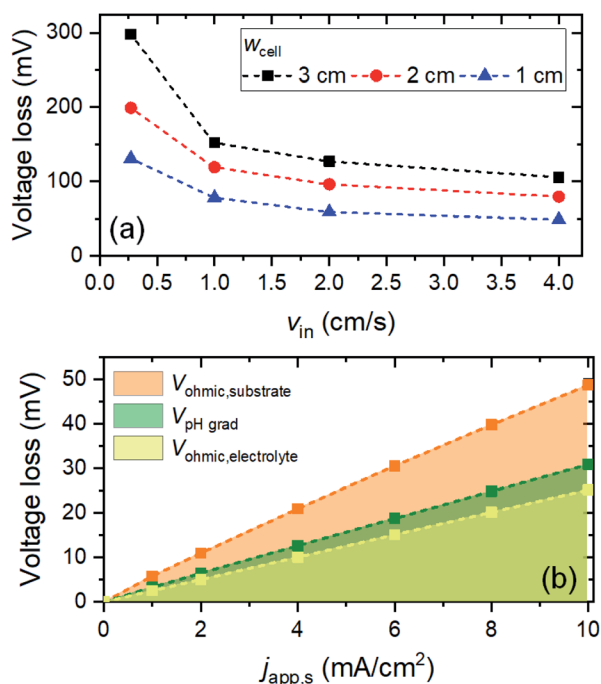
Fig. 6 (a) Total voltage losses for the 8 cm electrode with varying inlet velocities (v_{in}) and cell widths (w_{cell}); $j_{app,s} = 10$ mA cm^{-2}, $d_{contact} = 1$ cm. (b) Contribution of voltage losses at varying current densities; $w_{cell} = 1$ cm, $v_{in} = 4$ cm s^{-1}, $d_{contact} = 1$ cm. In all cases, the electrolyte is 2 M KP$_i$ buffer (pH 7), $h_{el} = 8$ cm, and $h_{cell} = 10$ cm.

will affect the pH gradient loss and product mixing. A particular example is bubble-induced convection; a recent study shows that an average bubble rise velocity of ~5 mm s^{-1} is obtained for a current density of 10 mA cm^{-2}.[48] To estimate the influence on the voltage loss, we adapted our model by including a volume force in the y-direction at the electrolyte regions close to the electrodes (0.2 mm, based on the reported average bubble diameter[48]), so that the electrolyte velocity in these regions is in the range of 4–6 mm s^{-1} (see Fig. S10†). Indeed, the main effect lies in the reduction of $V_{pH\,grad}$, while only minor variations are observed for $V_{ohmic,electrolyte}$ and $V_{ohmic,substrate}$. Multi-phase transport modeling considering bubble formation (which is dependent on surface roughness), aggregation and transport is needed to provide further details on its effect on the mass transport and mixing.

Conclusions

Using a two-dimensional Multiphysics model, we have identified various loss mechanisms related to scale-up in solar water splitting devices operating in neutral pH solutions. For an operating current density of 10 mA cm^{-2}, the total voltage loss increases from ~50 mV for a cell with an electrode height of 0.3 cm to ~600 mV for a cell with 8 cm electrode height. This includes substrate ohmic loss (~350 mV), pH gradient loss (~150 mV), and electrolyte ohmic loss (~100 mV). However, the application of relatively simple engineering strategies, such as the deposition of metallic lines on the substrate and adjusting

the operation/design parameters (*e.g.*, electrolyte flow rate, cell width), was found to be effective in overcoming these voltage losses. Combining all the presented strategies, a total voltage loss of only ~50 mV can be obtained, which is an acceptable level for the device operation. About half of this voltage loss is now due to the ohmic losses in the electrolyte. Other engineering strategies, such as the application of cell design (*e.g.*, using flow fields)[49–51] to optimize flow pattern or the use of electrolyte with higher conductivity (*e.g.*, operation at higher temperature to increase buffer solubility),[52–54] may be explored in order to further minimize the voltage loss. Finally, we note that our simulation results, which show non-linearity dependence between the electrode area and the total scale-up associated losses, qualitatively agree with experimental results reported in the literature.[21,23,55] Further experiments using – for example – *in situ* pH monitoring[56,57] and particle image velocimetry[58] are needed to quantitatively validate our findings.

Conflicts of interest

There are no conflicts to declare.

Acknowledgements

References

1 J. W. Ager, M. R. Shaner, K. A. Walczak, I. D. Sharp and S. Ardo, *Energy Environ. Sci.*, 2015, **8**, 2811–2824.

2 J. H. Kim, D. Hansora, P. Sharma, J.-W. Jang and J. S. Lee, *Chem. Soc. Rev.*, 2019, **48**, 1908–1971.

3 S. Tembhurne, F. Nandjou and S. Haussener, *Nat. Energy*, 2019, **4**, 399–407.

4 Solar PhotoElectroChemical Device Optimization, https://specdo.epfl.ch/.

5 J. Jia, L. C. Seitz, J. D. Benck, Y. Huo, Y. Chen, J. W. D. Ng, T. Bilir, J. S. Harris and T. F. Jaramillo, *Nat. Commun.*, 2016, **7**, 13237.

6 W.-H. Cheng, M. H. Richter, M. M. May, J. Ohlmann, D. Lackner, F. Dimroth, T. Hannappel, H. A. Atwater and H.-J. Lewerenz, *ACS Energy Lett.*, 2018, **3**, 1795–1800.

7 W. J. Chang, K.-H. Lee, H. Ha, K. Jin, G. Kim, S.-T. Hwang, H.-M. Lee, S.-W. Ahn, W. Yoon, H. Seo, J. S. Hong, Y. K. Go, J.-I. Ha and K. T. Nam, *ACS Omega*, 2017, **2**, 1009–1018.

8 S. A. Bonke, M. Wiechen, D. R. MacFarlane and L. Spiccia, *Energy Environ. Sci.*, 2015, **8**, 2791–2796.

9 M. Dumortier, S. Tembhurne and S. Haussener, *Energy Environ. Sci.*, 2015, **8**, 3614–3628.

10 J. H. Kim, J.-W. Jang, Y. H. Jo, F. F. Abdi, Y. H. Lee, R. van de Krol and J. S. Lee, *Nat. Commun.*, 2016, **7**, 13380.

11 F. F. Abdi, L. Han, A. H. M. Smets, M. Zeman, B. Dam and R. van de Krol, *Nat. Commun.*, 2013, **4**, 2195.

12 S. Kosar, Y. Pihosh, R. Bekarevich, K. Mitsuishi, K. Mawatari, Y. Kazoe, T. Kitamori, M. Tosa, A. B. Tarasov, E. A. Goodilin, Y. M. Struk, M. Kondo and I. Turkevych, *Appl. Nanosci.*, 2019, **9**, 1017–1024.

13 M. Kölbach, I. J. Pereira, K. Harbauer, P. Plate, K. Höflich, S. P. Berglund, D. Friedrich, R. van de Krol and F. F. Abdi, *Chem. Mater.*, 2018, **30**, 8322–8331.

14 F. F. Abdi and S. P. Berglund, *J. Phys. D: Appl. Phys.*, 2017, **50**, 193002.

15 S. P. Berglund, F. F. Abdi, P. Bogdanoff, A. Chemseddine, D. Friedrich and R. van de Krol, *Chem. Mater.*, 2016, **28**, 4231–4242.

16 K. Sivula and R. van de Krol, *Nat. Rev. Mater.*, 2016, **1**, 15010.

17 D. K. Lee, D. Lee, M. A. Lumley and K.-S. Choi, *Chem. Soc. Rev.*, 2019, **48**, 2126–2157.

18 M. Zhang, Y. Ma, D. Friedrich, R. van de Krol, L. H. Wong and F. F. Abdi, *J. Mater. Chem. A*, 2018, **6**, 548–555.

19 A. Vilanova, T. Lopes, C. Spenke, M. Wullenkord and A. Mendes, *Energy Storage Materials*, 2018, **13**, 175–188.

20 K. R. Tolod, S. Hernández and N. Russo, *Catalysts*, 2017, **7**, 13.

21 I. Y. Ahmet, Y. Ma, J.-W. Jang, T. Henschel, B. Stannowski, T. Lopes, A. Vilanova, A. Mendes, F. F. Abdi and R. van de Krol, *Sustainable Energy Fuels*, 2019, **3**, 2366–2379.

22 B. Turan, J.-P. Becker, F. Urbain, F. Finger, U. Rau and S. Haas, *Nat. Commun.*, 2016, **7**, 12681.

23 S. Dilger, M. Trottmann and S. Pokrant, *ChemSusChem*, 2019, **12**, 1931–1938.

24 I. Holmes-Gentle, H. Agarwal, F. Alhersh and K. Hellgardt, *Phys. Chem. Chem. Phys.*, 2018, **20**, 12422–12429.

25 M. R. Singh, K. Papadantonakis, C. Xiang and N. S. Lewis, *Energy Environ. Sci.*, 2015, **8**, 2760–2767.

26 C. Carver, Z. Ulissi, C. K. Ong, S. Dennison, G. H. Kelsall and K. Hellgardt, *Int. J. Hydrogen Energy*, 2012, **37**, 2911–2923.

27 S. Haussener, C. Xiang, J. M. Spurgeon, S. Ardo, N. S. Lewis and A. Z. Weber, *Energy Environ. Sci.*, 2012, **5**, 9922–9935.

28 M. A. Modestino, S. M. H. Hashemi and S. Haussener, *Energy Environ. Sci.*, 2016, **9**, 1533–1551.

29 D. V. Esposito, *Joule*, 2017, **1**, 651–658.

30 I. Holmes-Gentle, F. Hoffmann, C. A. Mesa and K. Hellgardt, *Sustainable Energy Fuels*, 2017, **1**, 1184–1198.

31 C. C. L. McCrory, S. Jung, I. M. Ferrer, S. M. Chatman, J. C. Peters and T. F. Jaramillo, *J. Am. Chem. Soc.*, 2015, **137**, 4347–4357.

32 C. C. L. McCrory, S. Jung, J. C. Peters and T. F. Jaramillo, *J. Am. Chem. Soc.*, 2013, **135**, 16977–16987.

33 S. Chen and L. W. Wang, *Chem. Mater.*, 2012, **24**, 3659–3666.

34 G. Lodi, E. Sivieri, A. De Battisti and S. Trasatti, *J. Appl. Electrochem.*, 1978, **8**, 135–143.

35 S. Trasatti, *J. Electroanal. Chem. Interfacial Electrochem.*, 1972, **39**, 163–184.

36 M. G. Walter, E. L. Warren, J. R. McKone, S. W. Boettcher, Q. Mi, E. A. Santori and N. S. Lewis, *Chem. Rev.*, 2010, **110**, 6446–6473.

37 K. Kinoshita, *Electrochemical oxygen technology*, John Wiley & Sons, 1992.

38 A. Battistel, C. R. Dennison, A. Lesch and H. H. Girault, *J. Phys. Chem. C*, 2019, **123**, 10849–10856.

39 I. A. Rauf, *J. Appl. Phys.*, 1996, **79**, 4057–4065.

40 I. A. Rauf, *J. Mater. Sci. Lett.*, 1993, **12**, 1902–1905.

41 M.-Z. Gao, R. Job, D.-S. Xue and W. R. Fahrner, *Chin. Phys. Lett.*, 2008, **25**, 1380–1383.

42 R. A. Serway and J. W. Jewett, *Principles of physics*, Saunders College Pub., Fort Worth, TX, 1998.

43 D. J. Griffiths, *Introduction to electrodynamics*, Prentice Hall, New Jersey, 1999.

44 Y. Pihosh, I. Turkevych, K. Mawatari, J. Uemura, Y. Kazoe, S. Kosar, K. Makita, T. Sugaya, T. Matsui and D. Fujita, *Sci. Rep.*, 2015, **5**, 11141.

45 R. Sheng, A. W. Y. Ho-Baillie, S. Huang, M. Keevers, X. Hao, L. Jiang, Y.-B. Cheng and M. A. Green, *J. Phys. Chem. Lett.*, 2015, **6**, 3931–3934.

46 S. Braun, R. Nissler, C. Ebert, D. Habermann and G. Hahn, *IEEE J. Photovolt.*, 2014, **4**, 148–153.

47 J. Jaus, H. Pantsar, J. Eckert, M. Duell, H. Herfurth and D. Doble, *35th IEEE Photovoltaic Specialists Conference*, 2010, pp. 000979–000983.

48 I. Holmes-Gentle, F. Bedoya-Lora, F. Alhersh and K. Hellgardt, *J. Phys. Chem. C*, 2019, **123**, 17–28.

49 Q. Xu, T. S. Zhao and C. Zhang, *Electrochim. Acta*, 2014, **142**, 61–67.

50 T. Jyothi Latha and S. Jayanti, *J. Appl. Electrochem.*, 2014, **44**, 995–1006.

51 A. Vilanova, T. Lopes and A. Mendes, *J. Power Sources*, 2018, **398**, 224–232.

52 W. M. Haynes, *CRC Handbook of Chemistry and Physics*, CRC Press, 2011.

53 P. Dias, T. Lopes, L. Andrade and A. Mendes, *J. Power Sources*, 2014, **272**, 567–580.

54 S. Haussener, S. Hu, C. Xiang, A. Z. Weber and N. S. Lewis, *Energy Environ. Sci.*, 2013, **6**, 3605–3618.

55 X. Yao, D. Wang, X. Zhao, S. Ma, P. S. Bassi, G. Yang, W. Chen, Z. Chen and T. Sritharan, *Energy Technol.*, 2018, **6**, 100–109.

56 B. Fuladpanjeh-Hojaghan, M. M. Elsutohy, V. Kabanov, B. Heyne, M. Trifkovic and E. P. L. Roberts, *Angew. Chem., Int. Ed.*, 2019, **58**, 16815–16819.

57 O. O. Talabi, A. E. Dorfi, G. D. O'Neil and D. V. Esposito, *Chem. Commun.*, 2017, **53**, 8006–8009.

58 R. Babu and M. K. Das, *Int. J. Hydrogen Energy*, 2019, **44**, 14467–14480.